Materials Today Bio 29 (2024) 101326

Contents lists available at ScienceDirect

Materials Today Bio

journal homepage: www.journals.elsevier.com/materials-today-bio

# Orchestrated copper-loaded nanoreactor for simultaneous induction of cuproptosis and immunotherapeutic intervention in colorectal cancer

Jiasheng Li [a,c,1], Shanshan Ma [a,1], Qiuhua Lin [a,c,1], Qin Wang [a], Wuning Zhong [a], Chunyin Wei [a], Junjie Liu [a], Jie Chen [a], Duo Wang [b,*], Weizhong Tang [a,c,**], Tao Luo [a,c,***]

[a] Department of Gastrointestinal Surgery, Department of Medical Ultrasound, Department of Breast, Bone & Soft Tissue Oncology, Day Oncology Unit and Department of Hepatobiliary Surgery, Guangxi Medical University Cancer Hospital, Guangxi Medical University, No. 71 Hedi Road, Nanning, 530021, China
[b] Center of Interventional Radiology & Vascular Surgery, Department of Radiology, Zhongda Hospital, Medical School, Southeast University, Nanjing, 224001, China
[c] Department of Guangxi Key Laboratory of Basic and Translational Research for Colorectal Cancer, Nanning, China

ARTICLE INFO

*Keywords:*
Colorectal cancer
Drug delivery system
Cuproptosis
Nanoreactor
cGAS-STING pathway
Immunotherapy

ABSTRACT

Ion interference, including intracellular copper (Cu) overload, disrupts cellular homeostasis, triggers mitochondrial dysfunction, and activates cell-specific death channels, highlighting its significant potential in cancer therapy. Nevertheless, the insufficient intracellular Cu ions transported by existing Cu ionophores, which are small molecules with short blood half-lives, inevitably hamper the effectiveness of cuproptosis. Herein, the ESCu@HM nanoreactor, self-assembled from the integration of H-$MnO_2$ nanoparticles with the Cu ionophore elesclomol (ES) and Cu, was fabricated to facilitate cuproptosis and further induce relevant immune responses. Specifically, the systemic circulation and tumoral accumulation of Cu, causing irreversible cuproptosis, work in conjunction with $Mn^{2+}$, resulting in the repolarization of tumor-associated macrophages (TAMs) and amplification of the activation of the cGAS-STING pathway by damaged DNA fragments in the nucleus and mitochondria. This further stimulates antitumor immunity and ultimately reprograms the tumor microenvironment (TME) to inhibit tumor growth. Overall, ESCu@HM as a nanoreactor for cuproptosis and immunotherapy, not only improves the dual antitumor mechanism of ES and provides potential optimization for its clinical application, but also paves the way for innovative strategies for cuproptosis-mediated colorectal cancer (CRC) treatment.

## 1. Introduction

Colorectal cancer (CRC) is currently the third-most common cancer in the world, resulting in diminished quality of life and placing a substantial economic burden on public health systems [1,2]. Although therapeutic advances such as surgical resection, radiotherapy, and other additional chemotherapy have yielded potential optimizations in both pre-clinical and clinical studies of CRC, their efficacy of destroying solid tumors in the preponderance of victims has been constrained (i.e., residual micro-metastases, radiation tolerance, chemotherapy drug resistance, and significant side effects) [3–5]. Immunotherapy, which serves as a remedial therapeutic measure by leveraging or enhancing the patient's immune system, has garnered worldwide attention since its emergence. Specifically, the immune checkpoint inhibitor pembrolizumab, an anti-PD1 antibody, has displayed remarkable efficacy in metastatic colorectal cancer (mCRC) with mismatch repair deficiency

* Corresponding author. Center of Interventional Radiology & Vascular Surgery, Department of Radiology, Zhongda Hospital, Medical School, Southeast University, Nanjing, 224001, China.
** Corresponding author. Department of Gastrointestinal Surgery, Department of Medical Ultrasound, Department of Breast, Bone & Soft Tissue Oncology, Day Oncology Unit and Department of Hepatobiliary Surgery, Guangxi Medical University Cancer Hospital, Guangxi Medical University, No. 71 Hedi Road, Nanning, 530021, China.
*** Corresponding author. Department of Gastrointestinal Surgery, Department of Medical Ultrasound, Department of Breast, Bone & Soft Tissue Oncology, Day Oncology Unit and Department of Hepatobiliary Surgery, Guangxi Medical University Cancer Hospital, Guangxi Medical University, No. 71 Hedi Road, Nanning, 530021, China.
*E-mail addresses:* wangduo2022@126.com (D. Wang), tangweizhong@gxmu.edu.cn (W. Tang), luotao@gxmu.edu.cn (T. Luo).
[1] These authors contributed equally to this work.

https://doi.org/10.1016/j.mtbio.2024.101326
Received 30 August 2024; Received in revised form 19 October 2024; Accepted 5 November 2024
Available online 9 November 2024

(dMMR) or high microsatellite instability (MSI-H) [6]. Unfortunately, the vast majority of CRCs are classified as "cold" tumors, characterized by microsatellite stability (MSS) or proficient mismatch repair (pMMR) status [7], which exhibit minimal to no response to anti-PD1 antibodies. Therefore, it is imperative to devise more effective treatment strategies that can address these limitations, minimize post-surgical tumor recurrence, concentrate therapeutic drugs at the tumor site, precisely eradicate residual tumor cells locally, and modulate the immunosuppressive tumor microenvironment (TME) to optimize the outcomes of immunotherapy.

The recently discovered mechanism of cuproptosis represents a promising strategy for tumor treatment. Benefiting from the significant up-regulation of cuproptosis-related gene expression levels in CRC, this emerging therapeutic approach is expected to be applied in CRC treatment. Apart from the high expression of cuproptosis-related genes, cuproptosis-related signatures, having been demonstrated, closely linked with immune cells infiltration in CRC, such as dendritic cells (DCs), $CD4^+$ or $CD8^+$ T cells and macrophages, both of which indicated that cuproptosis assisted by immune activation may improve the deficiencies in CRC therapy [8–11]. Cuproptosis, differing from established cell death modalities (i.e., ferroptosis, pyroptosis, or apoptosis), is uniquely identified by the accumulation of copper (Cu) ions and has emerged as a novel form of cellular demise [12–14]. In the mechanism of cuproptosis, Cu ions directly bind to lipoylated enzymes, vital components of the tricarboxylic acid cycle (TCA), prompting the aggregation of lipoylated proteins and the dissipation of iron-sulfur (Fe-S) cluster proteins, leading to proteotoxic stress and ultimately cell death. Intriguingly, the dramatic surge in toxic stress levels triggered by cuproptosis conspicuously facilitates the liberation of mitochondrial DNA (mtDNA) [15,16]. Furthermore, excessive Cu ions exhibit a proclivity for binding to nuclear DNA, which may further ignite the cGAS-STING signaling cascade, trigger the release of proinflammatory cytokines, and subsequently activate the innate immune response [17–19]. Nevertheless, the insufficient intracellular Cu ions transported by existing Cu ionophores, which are small molecules with short blood half-lives (i.e., disulfiram (DSF), 8-hydroxyquinoline (8-HQ), pyrithione), inevitably fail to effectively induce cuproptosis, which critically hinges on the sustained accumulation of Cu in mitochondria. Among the diverse Cu ionophores, elesclomol (ES), as a potential adjunct to chemotherapy, has garnered worldwide attention for its exceptional selectivity in transporting Cu directly into the mitochondria [20]. Despite its commendable safety profile, its poor biostability and undesirable side effects inevitably compromise its therapeutic potential. Hence, the quest for an optimal carrier that can augment the quantity of ES and bolster its circulatory stability is paramount in order to amplify the accumulation of Cu within tumor cells, ultimately enhancing the efficacy of cuproptosis-based CRC therapeutic strategies.

Hollow manganese dioxide (H-$MnO_2$) nanoparticles serve as a carrier and activator in immunotherapy, characterized by their unparalleled capability to encapsulate substantial quantities of ES and precisely respond to the specific TME [21,22]. Additionally, $MnO_2$ engages in redox reactions with glutathione (GSH), resulting in the production of glutathione persulfide (GSSH) and $Mn^{2+}$ [23], thereby synergistically augmenting the GSH depletion capability of $Cu^{2+}$, and ultimately safeguards the generation of reactive oxygen species (ROS). Concurrently, $Mn^{2+}$, liberating through the degradation of $MnO_2$, enhances the sensitivity of cGAS to double-stranded DNA (dsDNA) and its enzymatic activity, enabling cGAS to produce the secondary messenger cGAMP in the presence of low concentrations of dsDNA [24]. This further amplifies the activation of the cGAS-STING pathway in both tumor and immune cells induced by cuproptosis, thereby triggering the maturation of DCs, enabling them to effectively present tumor antigens and release anti-inflammatory substances, ultimately triggering a strong antitumor immune response.

Given the above considerations, we successfully designed and engineered the ESCu@HM nanoreactor by precisely manipulating atomic structures and electronic coordination environments. In this system, monodisperse H-$MnO_2$ with a homogeneous morphology was synthesized through the in situ growth of $MnO_2$ on solid silica nanoparticles, followed by the removal of the silica cores. Based on this, the ESCu@HM nanoreactor, self-assembled from the integration of H-$MnO_2$ nanoparticles with ES and Cu, was fabricated to trigger cuproptosis and provoke antitumor immunity (Scheme 1). The nanoparticles exhibited desirable physiological stability and controlled release behavior of ES, Cu, and $Mn^{2+}$ in response to the acidic tumor environment, following passive targeting via the enhanced permeability and retention (EPR) effect in CT26 tumor cells. In a nutshell, the liberated ES, which may concurrently efflux, chelate and transport additional extracellular Cu into cancer cells, along with Cu would trigger the aggregation of lipoylated dihydrolipoamide S-acetyltransferase (DLAT) and the destabilization of Fe-S cluster proteins, resulting in cuproptosis [25]. Notably, the released $Mn^{2+}$ could further enhance the sensitivity of the dsDNA sensor cGAS and amplify the activation of the STING pathway [24]. Ultimately, the simultaneous transformation of tumor-associated macrophages (TAMs) from the immunosuppressive M2 phenotype to the immunostimulatory M1 phenotype, along with the maturation of DCs and the infiltration of relevant T cells, is expected to reprogram the immunosuppressive TME and induce stronger antitumor immunity to inhibit CT26 tumor cells. In summary, the nanoreactor designed in this study can provide a potential optimization for ES clinical application and offer an innovative strategy for CRC treatment by inducing cuproptosis and enhancing cancer immunotherapy.

## 2. Materials and methods

### 2.1. Materials

Treaethyl orthosilicate (TEOS), ammonia solution (28 wt%), potassium permanganate ($KMnO_4$), sodium carbonate ($Na_2CO_3$) and copper (II) chloride dihydrate ($CuCl_2{\cdot}2H_2O$) were purchased from Aladdin Biochemical Technology Co., Ltd (Shanghai, China). Elesclomol (ES) was purchased from MedChemExpress (Shanghai, China). Fetal bovine serum (FBS), DMEM cell culture medium with high glucose, 0.25 % trypsin-EDTA and penicillin/streptomycin were purchased from Gibco BRL (Gaithersburg, MD, USA). Cell Counting Kit-8 (CCK-8), Live/Dead Cell Staining Kit, Hoechst 33342, 2′,7′-dichlorofluorescein diacetate (DCFH-DA), ATP assay kit, GSH assay kit and dialysis bag (MW 3.5 kDa cut-off) were purchased from Beyotime (Shanghai, China). Phosphate-buffered saline buffer (PBS), Annexin V-FITC/PI Kit and Copper (Cu) Detection Kit were acquired from Solaibao Technology Co., Ltd (Beijing, China). IL-6 ELISA kit, TNF-α ELISA kit and IFN-β ELISA kit were ordered from NeoBioscience Technology Co., Ltd (Shenzhen, China).

### 2.2. Synthesis and characterization of ESCu@HM

H-$MnO_2$ was synthesized by using solid silica nanoparticles ($sSiO_2$) as sacrificial hard templates. First, $sSiO_2$ nanotemplate was prepared by hydrolysis in alkaline solution with ethyl orthosilicate as precursor. Then an aqueous solution of $KMnO_4$ (300 mg) was dropwise added into the suspension of $sSiO_2$ (40 mg) under ultrasonication, and the brown $sSiO_2$@$MnO_2$ precipitate was obtained by centrifugation at 12000 rpm. To prepare the hollow-structured H-$MnO_2$, the prepared $SiO_2$@$MnO_2$ was dispersed in 2M $Na_2CO_3$ aqueous solution at 60 °C for 12 h. Subsequently, 4 mg ES and 4 mg H-$MnO_2$ were dissolved together in DMSO, and $CuCl_2{\cdot}2H_2O$ (11 mg) was added. The mixture was sonicated for 1 h at room temperature. After stirring for 12 h, the above solution was centrifuged and washed with water, and the obtained ESCu@HM was stored at 4 °C for future use. Utilizing ES and H-$MnO_2$ as the initial components, ES@HM was synthesized employing the identical method.

The morphology and elemental composition of nanoparticles were characterized by Transmission Electron Microscope (TEM, FEI Tecnai F20, USA). The size distribution and Zeta potential of nanoparticles was

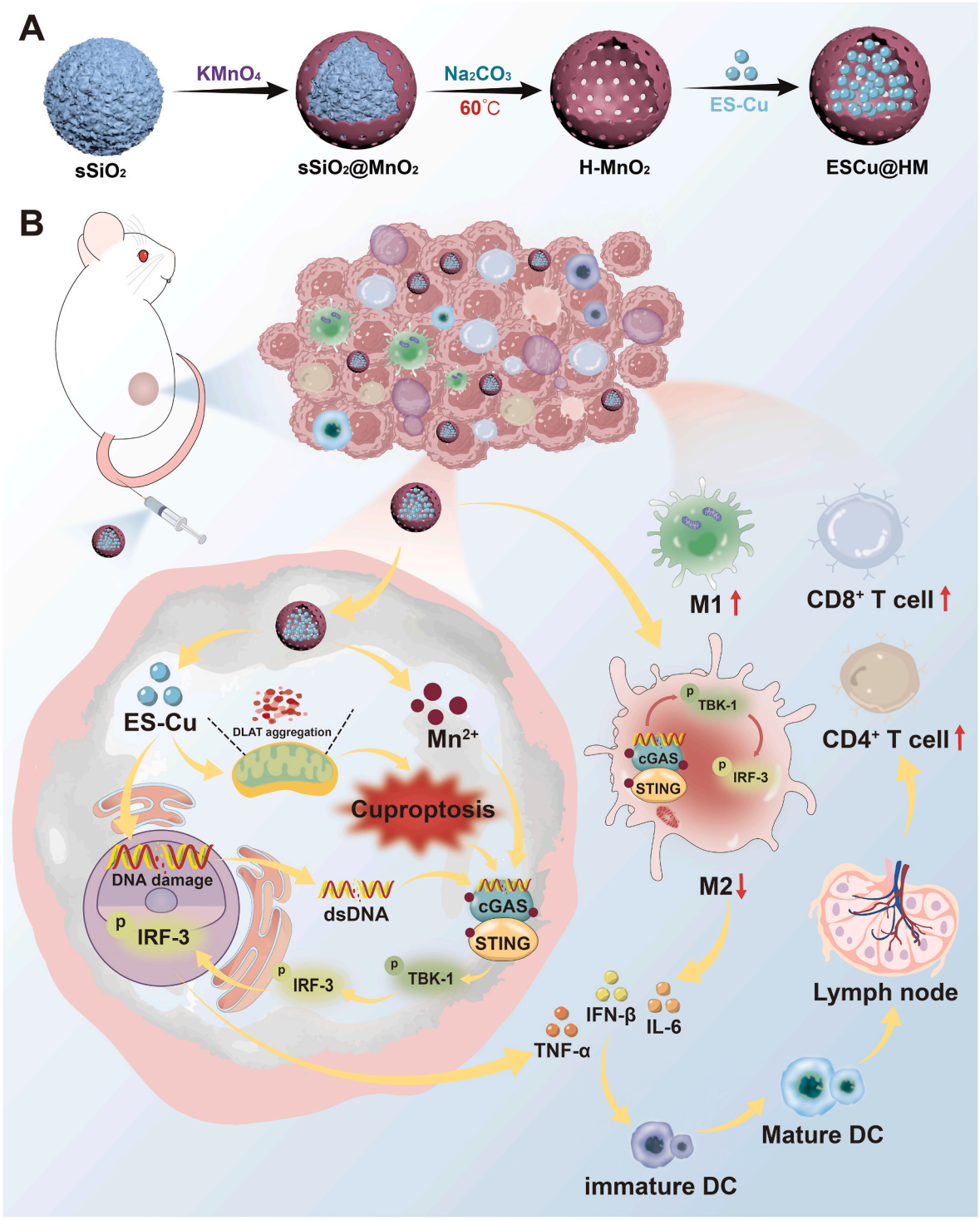


**Scheme 1.** Schematic Diagram of the Action of ESCu@HM. (A) Preparation of ESCu@HM; (B) Schematic illustration of ESCu@HM-induced cuproptosis and activation of the cGAS-STING pathway for colorectal cancer immunotherapy.

detected by Zetasizer Nano Analyzer (Malvern, UK). X-ray Photoelectron Spectroscopy (XPS) was performed using Thermo Escalab 250Xi (Thermo Fisher Scientific, USA). The loading capacity of ES was analyzed by High-performance liquid chromatography (HPLC).

### 2.3. Release of $Cu^{2+}$ from ESCu@HM

The dialysis method was adopted to study the release of $Cu^{2+}$ from ESCu@HM. In brief, ESCu@HM (1 mg/mL) was placed in a dialysis bag and then incubated with different PBS buffers (pH = 5.4 and 7.4) while gently shaking at 300 rpm at room temperature. At designated time points, the sample (1 mL) was taken and the released free $Cu^{2+}$ in the supernatant was quantified using ICP-MS (Perkin Elmer, USA).

### 2.4. Cell lines and animals

The CT26 cells and CT26-Luc cells were obtained from Haixing Biotechnology Co., Ltd (Suzhou, China). The RAW264.7 cells and THLE-

2 cells were acquired from China Center for Type Culture Collection (Wuhan, China). All cells have been verified through STR identification and cultured according to standardized methods.

4-week-old BALB/c mice were purchased from SPF (Beijing) Biotechnology Co., Ltd (Beijing, China), and were housed in a specific pathogen-free (SPF) animal facility. All animal experiments were approved by Guangxi Medical University Cancer Hospital's Ethical Committee. All experimental procedures were conducted in accordance with the Regulations for the Administration of Laboratory Animals approved by the State Council of the People's Republic of China.

### 2.5. Cellular uptake study

Cell culture slides were placed at the bottom of each well in a 24-well plate, and $1 \times 10^5$ CT26 cells were added to each well and incubated overnight at 37 °C. Subsequently, the cells were incubated with Cy5.5-labeled ESCu@HM (ESCu@HM@Cy5.5) for 0, 0.5 h, 1 h, 1.5 h and 2 h, respectively. Following incubation, the medium was removed, and the cells were washed three times with PBS before incubation with fresh medium. Then, the cells were stained with Hoechst 33342 for 15 min. After washing with PBS three times, the cells were imaged under a confocal laser scanning microscope (CLSM).

### 2.6. Measurement of intracellular Cu content

Measurement of intracellular Cu content using a Copper (Cu) Assay Kit. In brief, $1 \times 10^6$ CT26 cells were seeded in a 6-well plate and incubated overnight at 37 °C. Subsequently, the cells were treated with: (1) Control, (2) H-$MnO_2$, (3) ES, (4) ES@HM, (5) ESCu@HM. After another 6 h incubation, intracellular Cu content was measured using the kit according to the manufacturer's instructions.

### 2.7. Cytotoxicity assay

CT26 cells were seeded in 96-well plates at a density of $5 \times 10^3$ cells per well and incubated overnight. After that, the culture medium was replaced by the medium containing nanoparticles with a gradient concentration of ES (6.25, 12.5, 25, 50, 100 and 200 nM). Following 24 h of incubation, the cells were further incubated with CCK-8 solution for an additional 3 h and analyzed using a microplate reader (Tecan, Switzerland) at a wavelength of 450 nm. Additionally, the cytotoxicity of nanoparticles in the presence of $CuCl_2$ was also examined. In brief, $CuCl_2$ (0.1 μM or 1 μM) was added to the replacement medium, respectively.

### 2.8. Cell apoptosis assay

The apoptotic induction effect of nanoparticles was investigated using the Annexin V-FITC/PI apoptosis kit. In brief, CT26 cells were seeded into 6-well plates and incubated overnight. Subsequently, 0.1 μM $CuCl_2$ was added to the culture medium, followed by different treatments: (1) Control, (2) H-$MnO_2$, (3) ES, (4) ES@HM, (5) ESCu@HM. After another 12 h incubation, the cells were washed with PBS and collected into EP tubes. Subsequently, Annexin V-FITC and PI were added and analyzed using CytoFLEX flow cytometry (FCM, Beckman Coulter, USA).

### 2.9. Evaluation of cuproptosis pathway in vitro

Western blotting method was used to investigate the cuproptosis-related protein expression. Briefly, CT26 cells were seeded into 6-well plate and incubated overnight. 0.1 μM $CuCl_2$ was then added to the culture medium, followed by the addition of different nanoparticles and incubation for 12 h. RIPA cell lysate was used to extract the protein of cells, and the protein concentration was measured by an ultra-micro spectrophotometer (Gene Company Limited, China). Then, the loading buffer was added and heated for protein denaturation. The samples were added to sodium dodecyl sulfate-polyacrylamide gel electrophoresis (SDS-PAGE), and the proteins were transferred into the PVDF membrane. The PVDF membranes were blocked and successively incubated with primary antibodies and DyLight™ 680-labeled fluorescent secondary antibodies. The images were obtained by Odyssey DLx near-infrared dual-color laser imaging system (Gene Company Limited, China).

Additionally, for immunofluorescence (IF) analysis of cuproptosis-related protein, CT26 cells were seeded in a 24-well plate with coverslips and incubated overnight. 0.1 μM $CuCl_2$ was then added to the culture medium, followed by the addition of different nanoparticles and incubation for 12 h. The cells were sequentially fixed with 4 % paraformaldehyde, incubated overnight with primary antibody at 4 °C, followed by incubation with secondary antibodies for 1 h, stained with Hoechst 33342 for 15 min, and finally, images were captured using CLSM.

### 2.10. Measurement of intracellular glutathione

CT26 cells were seeded in a 6-well plate and incubated overnight. 1 μM $CuCl_2$ was added to the culture medium, followed by the addition of different nanoparticles. After 8 h of incubation, the culture medium was removed, and the cells were washed with PBS. Subsequently, the intracellular GSH level was evaluated using the GSH assay kit according to the manufacturer's instructions.

### 2.11. Detection of ROS generation in vitro

To detect intracellular ROS levels using DCFH-DA as a fluorescent probe. Briefly, CT26 cells were seeded into a 12-well plate and incubated overnight. 0.1 μM $CuCl_2$ was then added to the culture medium, followed by the addition of different nanoparticles and an 8 h incubation. Afterward, the cell culture medium was replaced with serum-free medium, and the cells were incubated with the ROS indicator DCFH-DA for 20 min. Subsequently, the cell nuclei were stained with Hoechst 33342. The fluorescence was observed under an inverted fluorescence microscope.

### 2.12. Live/dead cell staining assay

The cytotoxicity of diverse nanoparticles was investigated utilizing a Live/Dead assay kit. In brief, CT26 cells were cultured in a 12-well culture plate and grown for 24 h. Different nanoparticles and 0.1 μM $CuCl_2$ were added to the medium. After incubation for another 24 h, the cells were stained with PI (10 μg/mL) for 5 min in the dark, then stained with calcein-AM (5 μg/mL) for 10 min under the same conditions. Finally, images were taken under an inverted fluorescence microscopy.

### 2.13. Mitochondrial integrity assay

CT26 cells were seeded into confocal petri dishes and cultured overnight. After that, 1 μM $CuCl_2$ was then added to the culture medium, followed by the addition of different nanoparticles and incubation for 6 h. Then, the cells were stained with JC-1 dye according to manufacturer's instructions. Finally, the fluorescence images were recorded using CLSM.

### 2.14. Evaluation of intracellular ATP level

Intracellular ATP level was tested by the ATP assay kit. In brief, CT26 cells were inoculated into a 6-well plate and incubated overnight. 24 h after treatments, the intracellular ATP level was determined according to the manufacturer's protocol.

### 2.15. Detection of DNA damage

γ-H2AX IF analysis was used to detect DNA damage. CT26 cells were seeded into 24-well plates with coverslips and incubated overnight. 0.1 μM $CuCl_2$ was added to the medium, followed by the addition of different nanoparticles and incubation for 24 h. The cells were sequentially fixed with 4 % paraformaldehyde, permeabilized with 0.1 % Triton X-100, blocked with fast-acting blocking solution, incubated overnight at 4 °C with γ-H2AX antibody, incubated with the secondary antibody for 1 h at room temperature, stained with Hoechst 33342 for 15 min, and finally, images were captured using CLSM.

### 2.16. Evaluation of STING pathway activation

CT26 cells and RAW264.7 cells (Co-incubation with CT26 cells) were respectively cultured and treated as mentioned above for 12 h. Subsequently, to quantify the released cytokines (IFN-β, IL-6 and TNF-α), ELISA kits were employed to measure the cell culture supernatants after treatment with various nanoparticles, following the manufacturer's protocols. Additionally, western blotting and cellular IF techniques were utilized to investigate the activation status of relevant proteins in the STING pathway.

### 2.17. In vivo fluorescence imaging

CT26 cells ($2x10^6$ cells/mouse) were injected subcutaneously into the right flank of BALB/c mice to establish a CT26 tumor model. Tumor-bearing mice were then intravenously injected with Cy5.5-labeled ESCu@HM (ESCu@HM@Cy5.5). After injection, the mice were anesthetized at predetermined time points and observed using the infrared imaging system. For ex vivo biodistribution studies, mice were sacrificed 24 h post-injection, and their major organs (heart, liver, spleen, lung and kidney) as well as tumors were collected for imaging.

### 2.18. In vivo antitumor effect

To establish the CT26 tumor model, CT26-Luc cells ($2x10^6$ cells per mouse) were injected subcutaneously into the right flank of BALB/c mice. A total of 75 tumor-bearing mice were randomly divided into 5 groups (Control, H-$MnO_2$, ES, ES@HM and ESCu@HM) and received the designated treatments (ES concentration: 6 mg/kg) via tail vein injection on days 0, 3, 6, and 9. Tumor growth was carefully monitored using the in vivo imaging system (IVIS) (PerkinElmer, USA), and the tumor volume and body weight of each mouse were recorded every two days starting from the day of administration. Tumor volume was calculated using formula $V = (a \times b^2)/2$, where a and b represent the length and width of the tumor, respectively.

On the 16th day, 5 mice from each group were sacrificed, and an additional 10 mice per group were monitored for survival analysis. Tumors were collected from the sacrificed mice for weighing, photographing, and undergoing hematoxylin and eosin (H&E) staining, Ki67 immunohistochemistry (IHC) staining, and IF assays. Additionally, the expression of cuproptosis-related proteins was determined through western blotting and IHC analysis. Furthermore, relevant immune effects were investigated through FCM and ELISA analysis. Specifically, for FCM, primary tumors and tumor-draining lymph nodes (TDLNs) were isolated, and lymphocyte suspensions were stained with specific antibodies, including anti-CD11c-FITC, anti-CD80-PE and anti-CD86-APC, to analyze the maturity of DCs. Similarly, tumor homogenates were prepared and stained with anti-CD11b-PE, anti-F4/80-APC, anti-CD86-FITC and CD206-FITC antibodies to distinguish between M1 and M2 macrophage populations. Finally, serum samples from the mice were collected and analyzed using ELISA kits according to the manufacturer's instructions to detect cytokines, including IFN-β, IL-6, and TNF-α.

### 2.19. Measurement of hemolysis rate

Evaluation of the blood compatibility of ESCu@HM using red blood cells (RBCs). Mouse RBCs were incubated with different concentrations of ESCu@HM (6.25, 12.5, 25, 50, 100, 200, 300, 400, 500 μg/mL), with pure water as a positive control. After that, the supernatant was centrifugally collected (3500 rpm, 5 min) and the absorbance at 540 nm was measured through microplate reader.

### 2.20. Evaluation of vivo biological safety

In order to assess the bio-safety of ESCu@HM, healthy BALB/c mice were randomly divided into five groups (3 mice per group), and injected with PBS, H-$MnO_2$, ES, ES@HM and ESCu@HM via tail vein, respectively. The blood samples were collected on 16 day for blood routine test and blood biochemical analysis. Additionally, the mice were sacrificed to collect major organs (heart, liver, spleen, lung and kidney) for further analysis. All tissues were paraffin-embedded and prepared for histological sections. The tissue sections were stained with H&E to observe pathological features, and images were captured using an optical microscope.

### 2.21. Statistical analysis

Statistical analysis was performed using GraphPad Prism 8. Data are presented as mean ± standard deviation (SD). When comparing two groups, data were analyzed using Student's t-test. When comparing more than two groups, one-way or two-way analysis of variance (ANOVA) was used. Difference was considered to be significant if $P < 0.05$ (*$p < 0.05$, **$p < 0.01$, ***$p < 0.001$, ****$p < 0.0001$, ns indicates no significant).

## 3. Results and discussion

### 3.1. Preparation and characterization of ESCu@HM

As shown in Fig. 1A, the cuproptosis-mediated immunotherapy nanoreactor ESCu@HM was synthesized step by step. First, H-$MnO_2$ was synthesized according to a previously reported method [21]. Subsequently, ES and Cu were encapsulated into the H-$MnO_2$ to obtain ESCu@HM. ES@HM was also prepared by encapsulating ES in a similar manner. The TEM images clearly demonstrated that the synthesized H-$MnO_2$ exhibited a hollow structure with a uniform size distribution of approximately 120 nm. This size is located in the ideal dimension range of nanoparticles for EPR to take effect [26]. Moreover, the morphology of H-$MnO_2$ remained largely unchanged after encapsulation with ES and Cu (Fig. 1B). The elemental mapping images of Cu, Mn, N, O and S confirmed the successful preparation of ESCu@HM (Fig. 1C). Furthermore, XPS confirmed that ESCu@HM consists of Cu, Mn, N, O and S, further indicating that ESCu@HM was successfully prepared (Fig. 1D–F; Fig. S1, Supporting Information). In general, nanoparticles possessing both an adequate and stable particle size were favorably positioned to undergo systemic circulation and tumor accumulation. Consequently, the hydrodynamic sizes of s$SiO_2$@$MnO_2$, H-$MnO_2$, ES@HM, and ESCu@HM detected by dynamic light scattering (DLS) were approximately 126.7 nm, 132.5 nm, 142.5 nm, and 140.7 nm, respectively (Fig. 1G), representing an increase compared to s$SiO_2$ (107 nm). Meanwhile, ESCu@HM exhibited negligible aggregation or deposition in four different solutions at various time points (0, 6, 12, 24 h), and its particle size did not change significantly after 48 h of immersion in RPMI 1640 medium (Fig. S2, Supporting Information). In addition, the zeta potential analysis revealed that the prepared H-$MnO_2$ exhibited a negative potential (−31.5 mV), and the final product ESCu@HM still had a strong negative potential (−29.5 mV) (Fig. 1H). These results indicated that ESCu@HM possessed excellent dispersibility and stability in aqueous solutions.

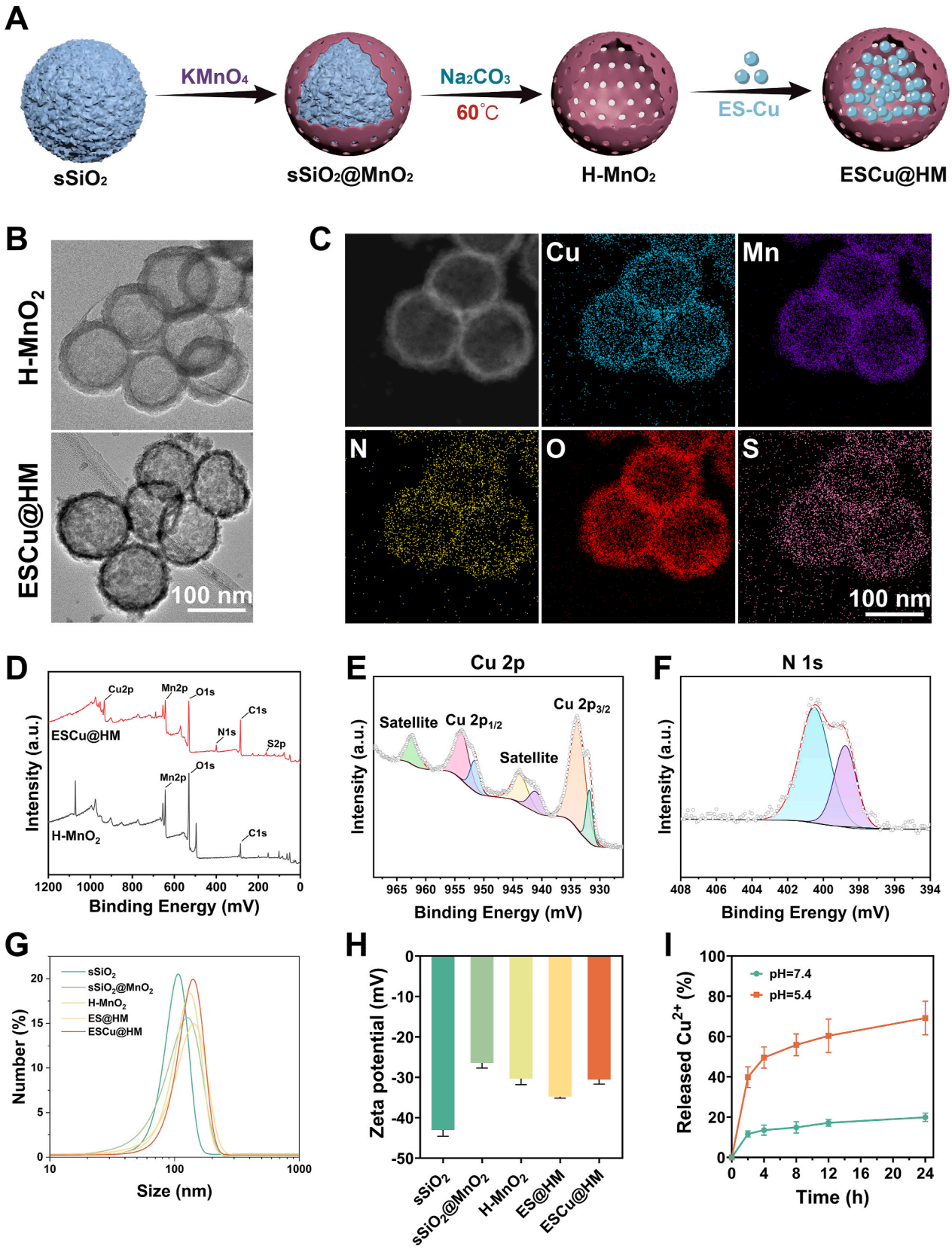


**Fig. 1.** Preparation and characterization of ESCu@HM nanoparticles. (A) Schematic illustration of the preparation of ESCu@HM. (B) TEM images of H-$MnO_2$ and ESCu@HM. (C) Elemental distribution mapping of ESCu@HM. (D–F) XPS spectra of full spectra (D), Cu 2p (E), and N 1s (F) of ESCu@HM. (G) Hydrated particle size of $sSiO_2$、$sSiO_2$@$MnO_2$、H-$MnO_2$、ES@HM and ESCu@HM in water. (H) Zeta-potential of $sSiO_2$、$sSiO_2$@$MnO_2$、H-$MnO_2$、ES@HM and ESCu@HM (n = 3). (I) Cumulative $Cu^{2+}$ release from ESCu@HM in PBS solution at pH 5.4 and pH 7.4 (n = 3).

It has been found that $MnO_2$ nanostructures would be decomposed by reaction with $H^+$ existing within the TME, generating $Mn^{2+}$ [21,27,28]. Therefore, acidic conditions can trigger the degradation of $MnO_2$, leading to the dissociation of ESCu@HM and the subsequent release of ES and Cu. This study explored the drug release capability of ESCu@HM under acidic conditions. As expected, the cumulative $Cu^{2+}$ release rate of ESCu@HM reached 69.19 % within 24 h at pH 5.4, while it was only around 19.92 % at pH 7.4 (Fig. 1I). This significant pH-dependent drug release behavior facilitates the targeted unloading of free drugs in the acidic tumor environment, thereby minimizing adverse side effects on normal tissues. These results not only further confirmed the successful formation of ESCu@HM but also demonstrated that ESCu@HM exhibits pH-sensitive drug release behavior, effectively releasing ES and Cu in the acidic tumor environment to exert their respective functions.

### 3.2. Cellular uptake and vitro cytotoxicity of ESCu@HM

To investigate the cellular uptake behavior of ESCu@HM in CT26 tumor cells, ESCu@HM was labeled with Cy5.5 dye (red) to form ESCu@HM@Cy5.5. The red fluorescence intensity of CT26 cells treated with

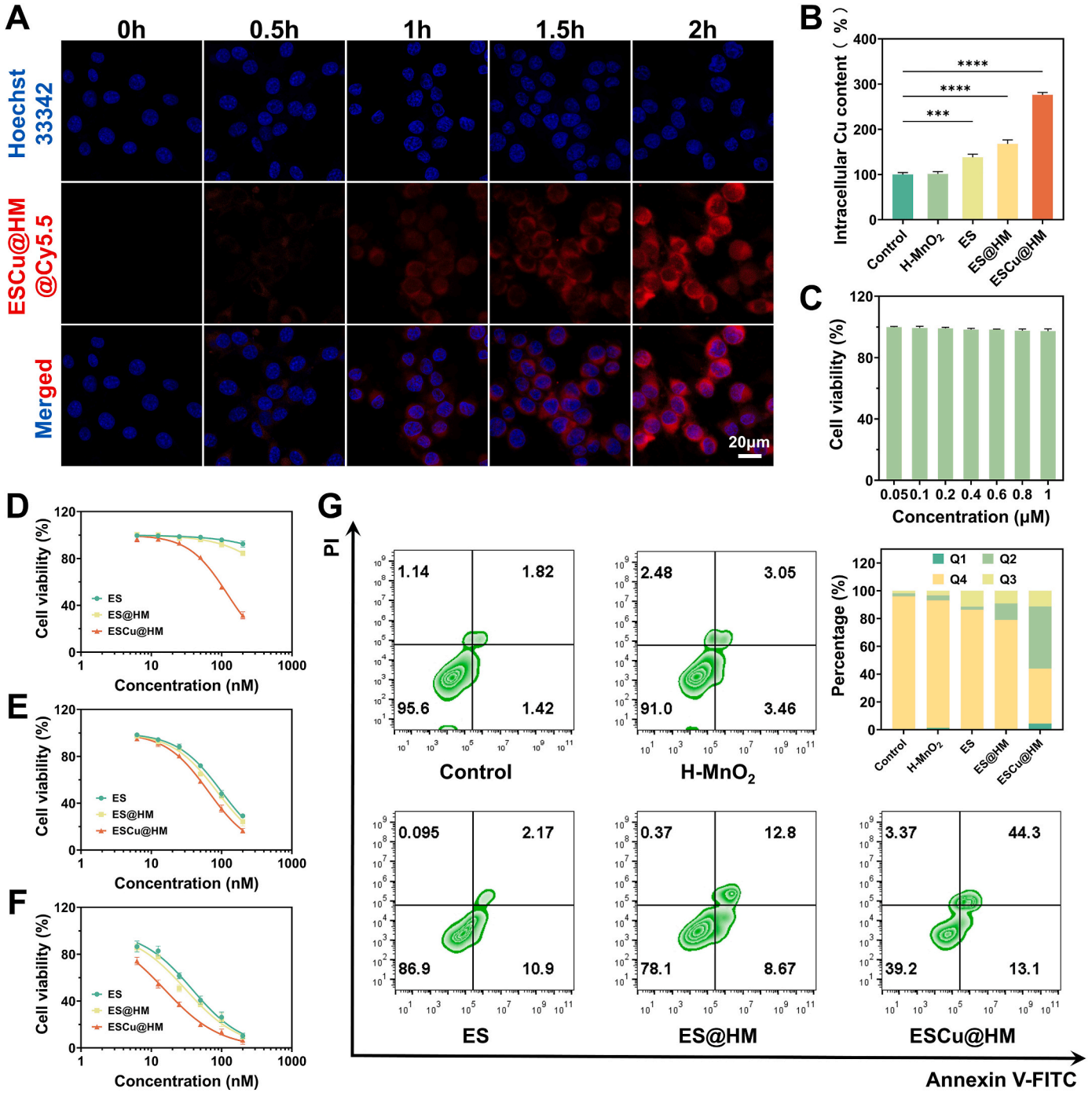


**Fig. 2.** Cellular uptake and in vitro cytotoxicity of ESCu@HM. (A) Representative CLSM images of CT26 cells stained with Cy5.5-labeled ESCu@HM. (B) The relative $Cu^{2+}$ content in CT26 cells with various treatments (n = 3). (C) In vitro cell cytotoxicity of $CuCl_2$ against CT26 tumor cell line (n = 3). (D–F) In vitro cytotoxicity of the nanoparticles against CT26 cell line without $CuCl_2$ (D), with 0.1 μM $CuCl_2$ (E) and 1 μM $CuCl_2$ (F), respectively (n = 3). (G) Annexin V-FITC and PI staining assays and the corresponding semi-quantitative analysis of CT26 cells after various treatments.

ESCu@HM@Cy5.5 was observed using CLSM at 0, 0.5, 1, 1.5 and 2 h. The results showed that the fluorescence intensity in CT26 cells gradually increased over time (Fig. 2A; Fig. S3, Supporting Information), indicating that the intracellular uptake of ESCu@HM by CT26 cells increased with the prolongation of nanoparticle incubation time.

ES, ES@HM and ESCu@HM all contain Cu ionophores capable of transporting $Cu^{2+}$ from the culture medium into cancer cells, potentially inducing cell death through cuproptosis. Among them, ESCu@HM, which includes both ES and Cu, is believed to have the strongest ability to transport $Cu^{2+}$ to tumor cells. The greater the amount of Cu transported into cells, the more likely it is to disrupt Cu homeostasis, thereby leading to cancer cell death through cuproptosis. Consequently, this study examined the intracellular Cu concentration in CT26 cells treated with ES, ES@HM and ESCu@HM to assess the efficiency of Cu transport. The results demonstrated a significant increase in the intracellular Cu content of CT26 cells treated with ESCu@HM, approximately 2.8 times higher than that of the control CT26 cells (Fig. 2B). This suggested that ESCu@HM can significantly enhance the transport of Cu into tumor cells, effectively disrupting Cu metabolic balance and leading to excessive accumulation of intracellular Cu.

Subsequently, the cytotoxicity of ESCu@HM against CT26 cells was evaluated in vitro using the CCK8 assay to assess its antitumor activity. As shown in Fig. 2D, the $IC_{50}$ values of ES and ES@HM were both above 200 nM, indicating that ES and ES@HM had almost no cytotoxicity. However, the $IC_{50}$ value of ESCu@HM was only 119.4 nM, suggesting that the incorporation of Cu significantly enhanced its antitumor capability. The Cu-loaded ESCu@HM effectively transported Cu into cells and eliminated cancer cells via cuproptosis. Furthermore, the antitumor effect of nanoparticles in the presence of $CuCl_2$ was also investigated. Firstly, the cytotoxicity of $CuCl_2$ was verified. The results showed that even at a concentration of 1 μM, $CuCl_2$ had little effect on the viability of CT26 cells (Fig. 2C). When CT26 cells were pre-incubated with 0.1 μM $CuCl_2$, the $IC_{50}$ values of ES, ES@HM and ESCu@HM were 99.52, 86.14 and 64.95 nM, respectively, all significantly lower than those without $CuCl_2$ pre-incubation (Fig. 2E). When the concentration of $CuCl_2$ pre-incubation increased to 1 μM, the $IC_{50}$ values of the nanoparticles further decreased (Fig. 2F), demonstrating a concentration-dependent relationship. In summary, ES, ES@HM and ESCu@HM can all transport extracellular Cu into cells and exhibit Cu-dependent antitumor activity. Notably, ESCu@HM demonstrated the highest cytotoxicity,

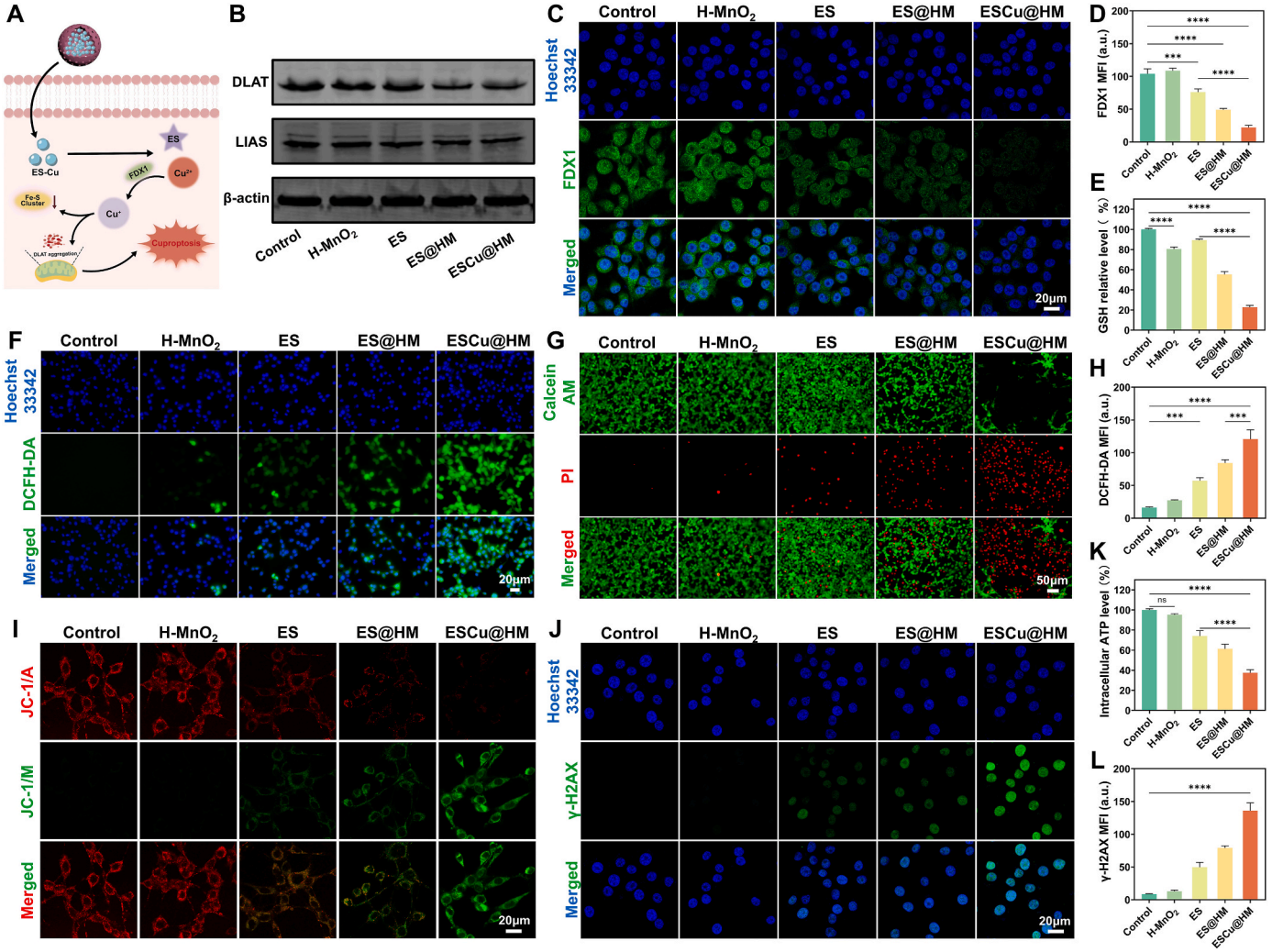


**Fig. 3.** ESCu@HM induced cuproptosis in vitro. (A) Schematic illustration of the possible mechanism of action of ESCu@HM in promoting cuproptosis. (B) Western blotting analysis of cuproptosis-related proteins expression. (C) Representative CLSM images of FDX1 in CT26 cells after various treatments. (D) Corresponding fluorescence statistics of FDX1 (n = 3). (E) Intracellular GSH contents after various treatments (n = 3). (F) Intracellular ROS level after treatment visualized by DCFH-DA. (G) Live/dead staining of CT26 cells after various treatments. Green and red fluorescence represented live and dead cells, respectively. (H) Corresponding fluorescence statistics of ROS (n = 3). (I) Mitochondrial membrane potentials of CT26 cells were determined by JC-1 assay after various treatments. (J) Representative CLSM images of γ-H2AX in CT26 cells after various treatments. (K) The levels of ATP in CT26 cells with various treatments (n = 3). (L) Corresponding fluorescence statistics of γ-H2AX (n = 3).

regardless of whether $CuCl_2$ pre-incubation was performed on cancer cells. Meanwhile, ESCu@HM exhibited negligible cytotoxicity against normal cells (Fig. S4, Supporting Information). Additionally, the apoptosis rate of CT26 cells treated with different drugs was explored using Annexin V-FITC and PI double staining to further assess the cytotoxicity of the nanoparticles. FCM analysis revealed that, under the same condition of 0.1 μM $CuCl_2$ treatment, the apoptosis rate of the ESCu@HM group was 57.4 %, which was 4.1 times that of the ES group (13.07 %) and 2.7 times that of the ES@HM group (21.47 %) (Fig. 2G). In conclusion, ESCu@HM possessed strong antitumor activity and was capable of effectively killing tumor cells in vitro.

### 3.3. Correlation analysis of cuproptosis induced by ESCu@HM

Previous studies have shown that cuproptosis is caused by intracellular Cu overload. On the one hand, Cu could trigger the protein oligomerization by binding to lipoylated DLAT. On the other hand, cuproptosis is also associated with the down-regulation of Fe-S cluster proteins, such as lipoyl synthase (LIAS) (Fig. 3A) [29,30]. Therefore, the expression of DLAT and LIAS as markers of cuproptosis was measured by western blotting. It was found that ES, ES@HM and ESCu@HM could effectively down-regulate the expression of DLAT and LIAS, especially ESCu@HM, suggesting that the nanoparticles could efficiently induce cell death via cuproptosis (Fig. 3B; Fig. S5, Supporting Information). In addition, ferredoxin 1 (FDX1) was identified as a key effector of DLAT lipoylation, capable of reducing $Cu^{2+}$ to $Cu^{+}$, leading to the increase in DLAT oligomers and subsequent cell death (Fig. 3A) [31,32]. IF analysis was employed to observe the expression of FDX1 in CT26 cells after various treatments. It could be seen that the expression was significantly reduced in the ESCu@HM group compared to the other groups (Fig. 3C and D). During cuproptosis, the increase in Cu content within tumor cells leads to significant depletion of GSH, which triggers a Fenton-like reaction of ROS accumulation. It has the potential to further induce oxidative stress and disrupt the redox homeostasis. Tumor cells are characterised by high redox homeostasis, and disrupting this balance has been proved to be a well-established therapeutic strategy [33,34]. Therefore, we detected the intercellular GSH and ROS levels. The intracellular GSH level was assessed using a GSH assay kit, revealing that, compared to the high GSH level in the control group, the GSH content in the other groups was reduced to varying degrees, with ES@HM and ESCu@HM performing better. This effect is thought to result from the simultaneous action of $MnO_2$ and $Cu^{2+}$ (Fig. 3E). After interacting with GSH, $Cu^{2+}$ is reduced to $Cu^{+}$ and reacts with $H_2O_2$ to form highly toxic hydroxyl radicals (·OH), which are also involved in the ROS generation process [35,36]. Furthermore, studies have indicated that ES can also produce ROS in tumor cells [37]. We therefore assessed the changes in intracellular ROS levels in CT26 cells pre-incubated with 0.1 μM of $CuCl_2$ and treated with different drugs using the fluorescent probe DCFH-DA. The results showed that CT26 cells treated with ESCu@HM exhibited the strongest green fluorescence compared to the almost negligible fluorescence in the control group, demonstrating that ESCu@HM possesses the best ROS production capacity (Fig. 3F–H). The above results suggested that cuproptosis, coupled with ROS production, effectively induces cell death. We also conducted a live/dead staining assay, which revealed that the highest number of dead cells (red) was found in CT26 cells treated with ESCu@HM (Fig. 3G), further demonstrating the combined anticancer effect of cuproptosis and amplified oxidative stress.

### 3.4. Antitumor immunity in vitro induced via ESCu@HM-Mediated cuproptosis

In light of the outstanding performance of ESCu@HM-mediated cuproptosis in CT26 tumor cells, we further explored the link between ESCu@HM-mediated cuproptosis and immune response. Previous studies have indicated that the elevation of protein toxicity stress caused by cuproptosis and ROS accumulation can lead to mitochondrial damage, promoting the release of mtDNA [33,38]. The released cytoplasmic dsDNA can directly activate the STING pathway, thereby triggering the immune response [18,39]. Furthermore, it has been demonstrated that free $Mn^{2+}$ could amplify STING activation [40,41]. $Mn^{2+}$ enhances the sensitivity of the dsDNA sensor cGAS, effectively amplifying the activation of the STING pathway in both tumor and immune cells. This subsequently initiates downstream signaling events through the recruitment and activation of TBK1 and IRF3, further coordinating innate and adaptive immunity to exert antitumor effects [24,42,43]. Therefore, we evaluated the ability of ESCu@HM to activate the STING pathway ex vivo.

The JC-1 probe was first employed to validate the associated mitochondrial damage. JC-1 is a physiological marker used to assess mitochondrial function and track changes in mitochondrial membrane potential. It forms red-fluorescent J-aggregates in normal mitochondria and conversely green-fluorescent monomers in damaged mitochondria. The results showed that ESCu@HM treatment up-regulated the green fluorescent monomer signals of JC-1 while down-regulated its red signals compared to other treatment groups (Fig. 3I; Fig. S6, Supporting Information). This suggests that cuproptosis and oxidative stress mediated by the nanoparticles effectively induce mitochondrial dysfunction, causing J-aggregates in mitochondria to leak out and become monomers diffusing in the cytoplasm. Mitochondrial disruption was further confirmed by a reduction of intracellular ATP levels (Fig. 3K). Notably, the intracellular ATP levels in RAW264.7 cells treated with different drugs were not significantly reduced, indicating that ESCu@HM does not cause damage to mitochondria in normal immune cells (Fig. S7, Supporting Information). Moreover, excess intracellular Cu binds to DNA in the nucleus, leading to DNA damage [17]. The DNA-damaging effect of ESCu@HM was evident from γ-H2AX IF staining (Fig. 3J–L).

Next, we evaluated the ability of ESCu@HM to activate the STING pathway in vitro (Fig. 4A). Upon activation, the STING pathway initiates downstream signal transduction events by recruiting and activating TBK1 and IRF3, which induce the expression and secretion of IFN-β and pro-inflammatory cytokines, such as IL-6 and TNF-α [44,45]. Therefore, after co-incubation with different treatments, ELISA kits were used to measure the expression levels of IFN-β, IL-6 and TFN-α in the CT26 cell culture supernatant. The results showed that the levels of these cytokines in the supernatant increased following treatment with ES, ES@HM, and ESCu@HM, particularly in the ESCu@HM group, which exhibited the most significant increase (Fig. 4B–D). This indicates that ESCu@HM effectively activates the STING pathway in CT26 cells. Furthermore, we observed similar results in RAW264.7 cells (Fig. 4E–H), suggesting that ESCu@HM can also activate the STING pathway in these immune cells, initiating innate immunity to block tumor escape and stimulate adaptive immunity. Subsequently, IF detection was performed on STING pathway-related proteins (cGAS, p-STING and p-IRF3) in both CT26 and RAW264.7 cells. The results revealed that the fluorescence signals in the ES, ES@HM, and ESCu@HM groups gradually increased, indicating significant up-regulation of cGAS, p-STING and p-IRF3, particularly in the ESCu@HM group (Fig. 4I and J; Fig. S8, Supporting Information). Additionally, western blotting results showed similar trends (Fig. 4K and L; Figs. S9 and S10, Supporting Information). These results demonstrated the activation of the STING pathway in both CT26 and RAW264.7 cells. Notably, H-$MnO_2$ only increased the levels of p-STING or p-TBK1 and had minimal effect on the expression of cGAS and p-IRF3 compared to the control group. This may be due to its inability to induce DNA damage at low concentrations, thus preventing the triggering of downstream signaling events such as the activation of p-IRF3. Meanwhile, ES@HM induced a greater number of phosphorylated proteins related to the STING pathway than ES. We speculated that the sensitization of the STING pathway by $Mn^{2+}$ in ES@HM plays a role in this effect.

In summary, ESCu@HM effectively induces nuclear and mitochondrial DNA damage in tumor cells, leading to the release of DNA

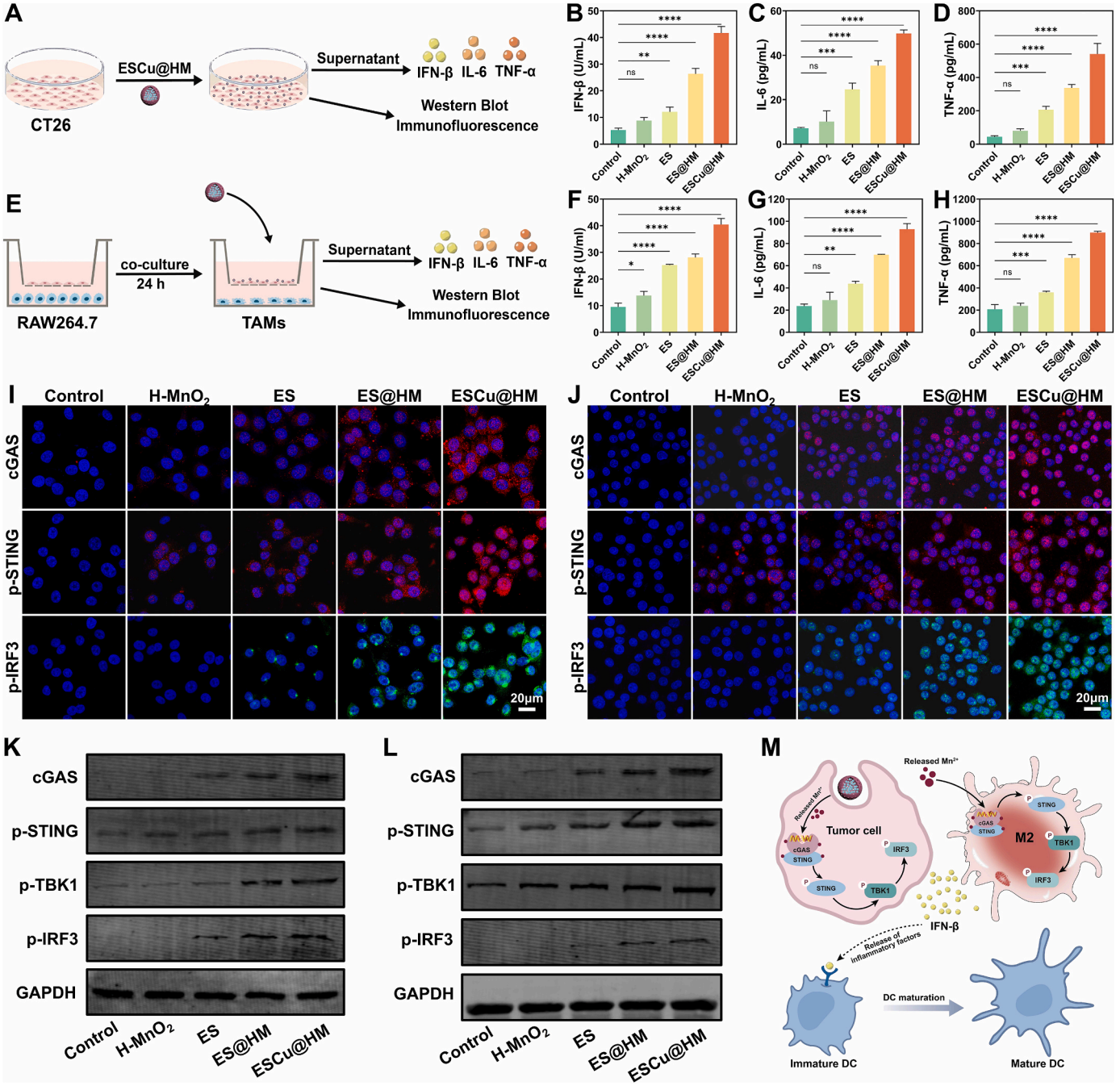


**Fig. 4.** Activation of the cGAS-STING pathway by ESCu@HM. (A) Schematic in vitro experimental procedure of the STING pathway activation in CT26 cells. The secretion levels of (B) IFN-β、(C) IL-6 and (D) TNF-α in the supernatant of CT26 cells after various treatments (n = 3). (E) Schematic in vitro experimental procedure of the STING pathway activation in RAW264.7 cells. The secretion levels of (F) IFN-β、(G) IL-6 and (H) TNF-α in the supernatant of RAW264.7 cells after various treatments (n = 3). (I) Representative CLSM images of cGAS, p-STING and p-IRF3 in CT26 cells after various treatments. (J) Representative CLSM images of cGAS, p-STING and p-IRF3 in RAW264.7 cells after various treatments. (K) Western blot detection of the STING pathway-related proteins in CT26 cells. (L) Western blot detection of the STING pathway-related proteins in RAW264.7 cells. (M) Schematic diagram of the cGAS-STING pathway activation by ESCu@HM.

fragments into the cytoplasm. With the amplification of $Mn^{2+}$, the cGAS-STING pathway is effectively activated, promoting systemic antitumor immunity. Similar events also occur in immune cells, such as macrophages, where the cGAS-STING-TBK1 pathway is activated, resulting in a stronger immune response to inhibit tumor cells (Fig. 4M). This indicates that ESCu@HM-mediated cuproptosis could play a significant role in immunotherapy.

### 3.5. Biocompatibility and biodistribution of ESCu@HM

The in vivo toxicity of nanomedicines is a crucial factor affecting their clinical application [46], so we evaluated the biocompatibility of ESCu@HM. First, the blood compatibility of ESCu@HM was assessed using a hemolysis assay. When red blood cells were incubated with various concentrations of ESCu@HM, the hemolysis rate was less than 5 % (Fig. S11, Supporting Information), indicating satisfactory blood compatibility. Moreover, we injected PBS, H-$MnO_2$, ES, ES@HM and ESCu@HM (at a total dose of 6 mg ES/kg) into healthy mice via the tail

vein for four consecutive times. Blood samples and major organs from mice treated with different drugs were collected on the 16th day for further analysis. The results showed no significant differences in hematological indicators among all treatment groups compared to the control group, with all values remaining within the normal range (Fig. S12, Supporting Information). Next, the main organs of the mice (heart, liver, spleen, lung, kidney) were examined using H&E staining. Similarly, no obvious morphological changes were observed in the major organs of any treatment group compared to the control group (Fig. S13, Supporting Information). In summary, ESCu@HM exhibited negligible side effects and satisfactory biocompatibility.

Afterward, we constructed a subcutaneous animal model of colon cancer based on CT26 cells, and further studied the in vivo biodistribution and tumor accumulation of ESCu@HM by the infrared imaging system. Cy5.5-labeled ESCu@HM (ESCu@HM@Cy5.5) was injected into tumor-bearing mice via the tail vein, and the fluorescence signal was monitored by the infrared imaging system at designated time points. The results indicated that the fluorescence signal accumulated in the tumor area 2 h after the injection of ESCu@HM@Cy5.5, with fluorescence intensity continuing to increase over time, peaking around 12 h, and slightly diminishing at 24 h (Fig. 5A; Fig. S14A, Supporting Information). This suggests that ESCu@HM@Cy5.5 can rapidly accumulate at the tumor site and achieve long-term retention, ascribed to the EPR effect. In addition, mice were sacrificed at 24 h after the injection of ESCu@HM@Cy5.5, and the tumors and major organs (heart, liver, spleen, lung, kidney) were removed to study the ex vivo biodistribution. The results showed pronounced fluorescence signals in both the tumor and liver, indicating that ESCu@HM prepared in this study not only exhibited effective passive tumor homing after systemic administration via the EPR effect but was also rapidly metabolized by the liver (Fig. 5B; Fig. S14B, Supporting Information). Herein we speculated that ESCu@HM could effectively improve the half-life of ES and enhance its circulation stability, which is extremely favourable for its clinical application.

### 3.6. In vivo antitumor performance of ESCu@HM

Inspired by the impressive in vitro therapeutic effect observed, we constructed a subcutaneous tumor model based on CT26-Luc cells to evaluate the antitumor efficacy induced by ESCu@HM in vivo. Tumor-bearing mice were randomly divided into 5 groups (PBS, H-$MnO_2$, ES, ES@HM and ESCu@HM) and received the indicated treatments on days 0, 3, 6 and 9 (Fig. 5C). Tumor volumes and body weights of the mice were recorded and analyzed every other day from the date of administration (Fig. 5D–F), and tumor growth was carefully monitored using the IVIS (Fig. 5G). Tumors were excised, weighed and photographed on day 16 (Fig. 5H; Fig. S15, Supporting Information). Only slight antitumor effects were observed in the H-$MnO_2$ and ES groups compared to the control group. In contrast, the ES@HM group demonstrated notable antitumor efficacy, suggesting that ES@HM effectively increased the in vivo circulation time and tumor retention capacity of ES. As expected, ESCu@HM exhibited the strongest antitumor effect, indicating that the increase in Cu can effectively activate cuproptosis and thus inhibit the growth of tumors in vivo. Meanwhile, the body weights of mice treated with different drugs changed, but there was no statistical difference between the groups, further suggesting that ESCu@HM has weak systemic toxicity. In addition, the survival rate of the mice was assessed, revealing that ESCu@HM treatment significantly improved the survival time of tumor-bearing mice compared to the other groups (Fig. 5I). The expression of cuproptosis-related proteins in the tumors was further examined using western blotting and IHC analysis (Fig. 5J; Figs. S16 and S17, Supporting Information). As expected, the loss of LIAS and FDX1, as well as the aggregation of DLAT, was observed in tumors treated with ES, ES@HM and ESCu@HM, confirming the effective activation of cuproptosis in vivo. Among these treatments, ESCu@HM exhibited the most potent ability to induce cuproptosis. Moreover, H&E staining of tumor tissues revealed more extensive nuclear fragmentation and nucleolysis in tumor cells of ESCu@HM-treated mice compared to those treated with other drugs (Fig. 5K). The results of Ki67 IHC staining also confirmed that ESCu@HM inhibited the expression of Ki67, indicating a reduction in the proliferation of tumor cells (Fig. 5K). Taken together, these results suggest that ESCu@HM has excellent antitumor effects in vivo and can effectively inhibit tumor growth.

### 3.7. Cuproptosis-mediated in vivo immune activation

To assess ESCu@HM-mediated immune responses in vivo, tumors and tumor-draining lymph nodes (TDLNs) from mice treated with different drugs were collected for immune parameter analysis to further evaluate its antitumor immunity. The activation of the STING pathway promotes the maturation of DCs [47,48], thus we investigated the maturation of DCs in TDLNs of the mice using FCM. The results showed that the percentage of mature DCs ($CD80^+CD86^+$) increased to 25.7 % in ESCu@HM-treated mice, significantly higher than the 6.21 % observed in the control group (Fig. 6A and B). In addition, we observed a greater infiltration of DCs in the tumor tissues of the ESCu@HM group (Fig. 6C; Fig. S18, Supporting Information). These results indicate that ESCu@HM significantly increased DC infiltration in tumor tissues and effectively promoted DC maturation. Meanwhile, we measured the expression levels of IFN-β, IL-6 and TNF-α in mouse serum using ELISA kits and found that ESCu@HM enhanced the expression of these cytokines more efficiently than PBS, H-$MnO_2$, ES, and ES@HM (Fig. 6D–F). The higher expression levels suggest that ESCu@HM resulted in stronger in vivo activation of the STING pathway, which better promotes DC maturation and activates antitumor immunity. Previous studies have shown that mature DCs have an efficient antigen-presenting ability to present antigens to T cells, stimulating naïve T cells to proliferate and infiltrate tumor tissues to kill cancer cells [49,50]. Therefore, we analyzed the infiltration of T cells. IF staining images of $CD4^+$ and $CD8^+$ T cells in tumor tissues demonstrated that ESCu@HM significantly increased the infiltration of both $CD4^+$ and $CD8^+$ T cells in tumor tissues (Fig. 6G and H; Fig. S19, Supporting Information). Collectively, these results indicate that ESCu@HM is capable of stimulating a robust immune response in vivo through the activation of the STING pathway.

TAMs are important components of the immune system that surround and interact with tumor cells, regulate the TME, and are closely associated with tumor proliferation, extracellular matrix remodeling, and tumor immune tolerance [51,52]. Activated macrophages can be classified into M1-type and M2-type macrophages. M1-type macrophages ($CD11b^+F4/80^+CD86^+$) promote T-cell activity by secreting pro-inflammatory cytokines and chemokines and presenting antigens. In contrast, M2-type macrophages ($CD11b^+F4/80^+CD206^+$) exhibit immunosuppressive properties, inhibiting T-cell proliferation and inducing tumor immune escape [53,54]. To determine whether ESCu@HM could induce the repolarization of M2-type macrophages into M1-type macrophages and thereby improve the TME, we explored the polarization of TAMs in tumor tissues using FCM. The results showed that the proportion of M1-type macrophages in the tumors of mice treated with ESCu@HM was significantly higher than that in mice treated with other drugs (Fig. 6I; Fig. S20, Supporting Information). Meanwhile, the proportion of M2-type macrophages in the tumors of mice treated with ESCu@HM was significantly lower than that in other treatment groups (Fig. 6J; Fig. S21, Supporting Information). Furthermore, we found that the M1/M2 ratio increased significantly in the ESCu@HM treatment group (Fig. 6K). These results suggest that ESCu@HM can induce the repolarization of TAMs from M2-type to M1-type macrophages. Therefore, we propose that the in vivo antitumor immunity induced by ESCu@HM-mediated cuproptosis can effectively reprogram the TME to exert more potent antitumor effects.

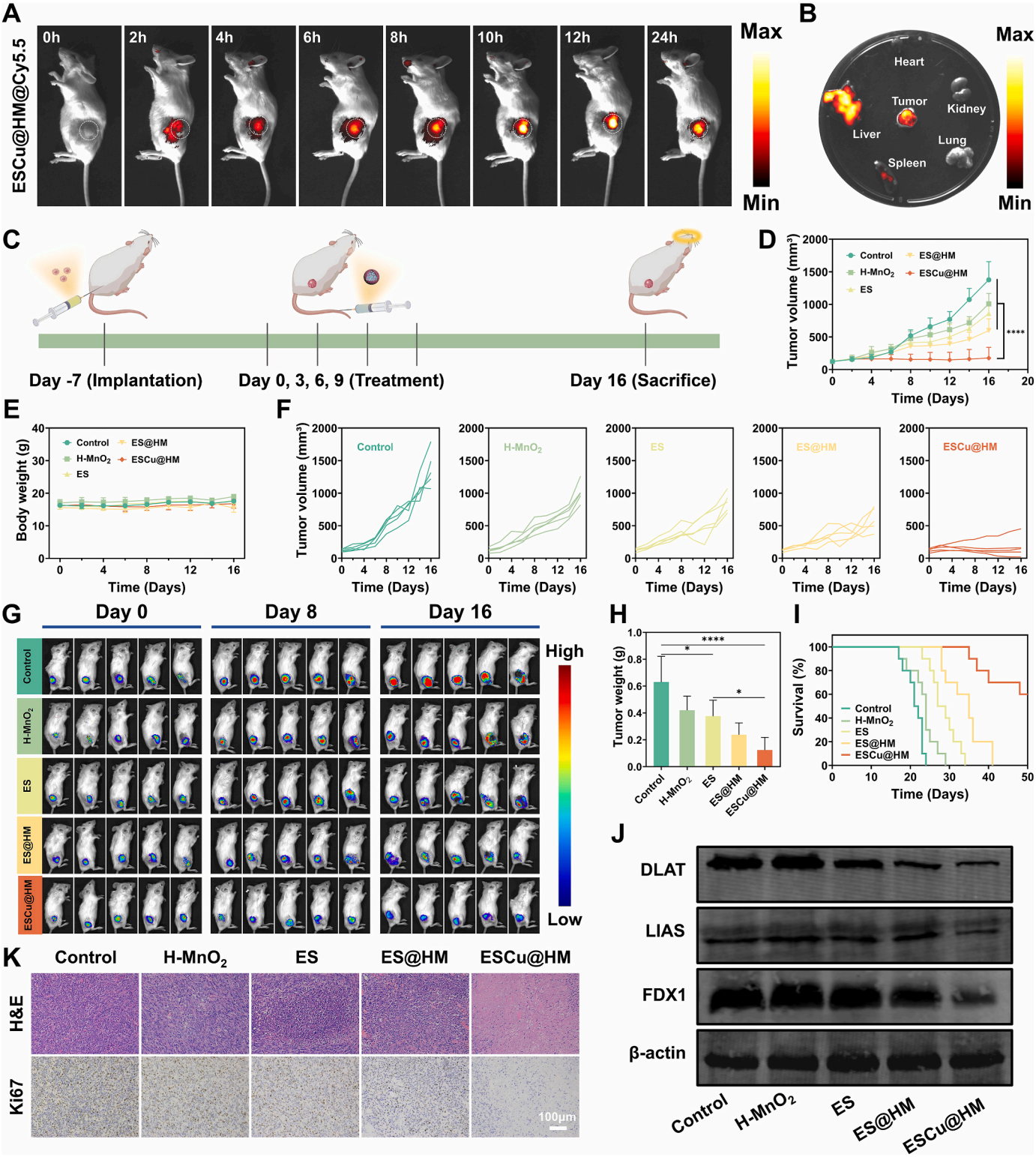


**Fig. 5.** Evaluation of antitumor effect mediated by ESCu@HM in CT26 tumor-bearing mice. (A) Biodistribution after intravenous injection of ESCu@HM@Cy5.5 at different time points. (B) Ex vivo fluorescence images of tumor and major organs including heart, liver, spleen, lung and kidney collected at 24 h post-injection. (C) Schematic illustration of the experimental schedule for subcutaneous CT26 tumor model treatment. (D) Changes in mice tumor volumes (n = 5). (E) Body weight changes in treated mice (n = 5). (F) Individual tumor growth curves of mice post various treatments. (G) Luminescence images of tumor-bearing mice at day 0, day 8 and day 16, respectively, through IVIS. (H) Tumor weight at day 16 in five groups (n = 5). (I) Survival curves of tumor-bearing mice in different groups within 50 days (n = 10). (J) Intratumoral cuproptosis-related proteins expression with various treatments, observed by western blotting. (K) H&E– and Ki67-stained images of tumor tissues from all groups.

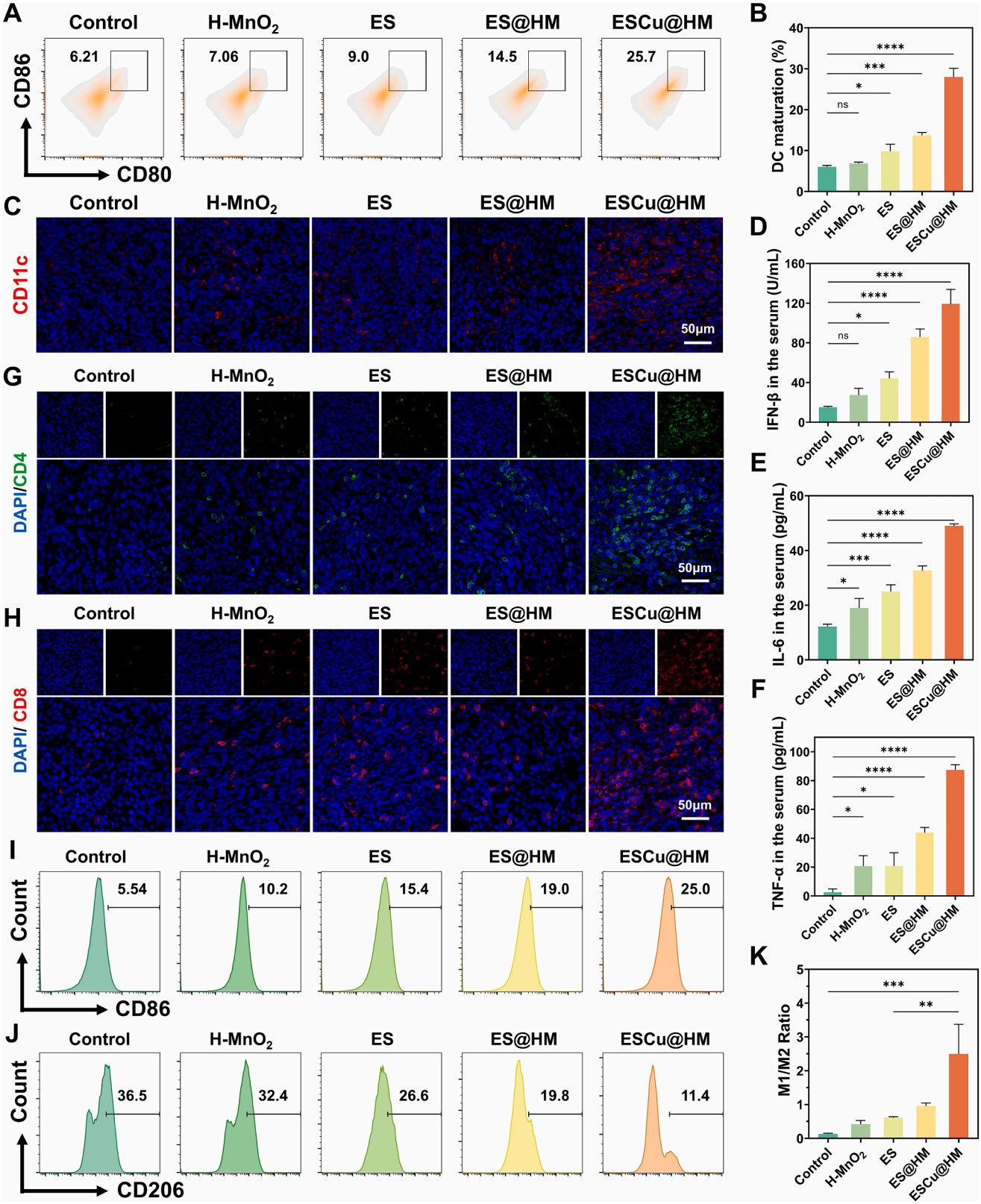


**Fig. 6.** Assessment of antitumor immunity mediated by ESCu@HM in vivo. (A) Flow cytometry analysis of $CD80^+/CD86^+$ subpopulation of mature DCs in lymph nodes. (B) Histogram analysis of the percentages of matured DCs (n = 3). (C) Immunofluorescence images of DCs ($CD11c^+$) in tumor sections. (D–F) The expression levels of (D) IFN-β、(E) IL-6 and (F) TNF-α in the serum (n = 3). (G) Immunofluorescence images of $CD4^+$ T cells in tumor sections. (H) Immunofluorescence images of $CD8^+$ T cells in tumor sections. (I) Typical flow cytometry analysis of M1 macrophages in tumors. (J) Typical flow cytometry analysis of M2 macrophages in tumors. (K) M1/M2 ratio in tumor tissues (n = 3).

## 4. Conclusions

Briefly, this study constructed ESCu@HM nanoreactor as a pH-responsive drug delivery nanoplatform, which significantly improved the in vivo cycling and tumor accumulation of ES, enabling cancer cells to be sensitive to cuproptosis and activate cuproptosis-mediated antitumor immunity. After cellular uptake, ESCu@HM rapidly degraded in an acidic environment and released ES, $Cu^{2+}$ and $Mn^{2+}$, which continually increased the accumulation of Cu to further induce cuproptosis and simultaneously activated cGAS-STING pathway in tumor and immune cells to further educate TAMs into pro-inflammatory M1-type macrophages, stimulate DC activation, and T cell infiltration, and ultimately reversing the immunosuppressive tumor microenvironment to boost effective antitumor effect without obvious toxicity. Of note, the excellent biocompatibility ensures the high clinical translation potential of such sequential nanoreactor, which is expected to provide a more effective and safe therapeutic strategy for synergistic treatment of CRC and more other tumors.

## CRediT authorship contribution statement

**Jiasheng Li:** Writing – original draft, Data curation, Conceptualization. **Shanshan Ma:** Software, Methodology. **Qiuhua Lin:** Validation, Methodology, Conceptualization. **Qin Wang:** Investigation, Formal analysis. **Wuning Zhong:** Resources. **Chunyin Wei:** Funding acquisition. **Junjie Liu:** Funding acquisition. **Jie Chen:** Funding acquisition. **Duo Wang:** Funding acquisition. **Weizhong Tang:** Project administration, Funding acquisition. **Tao Luo:** Writing – review & editing, Visualization, Supervision, Project administration, Conceptualization.

## Informed consent statement

Not applicable.

## Institutional review board statement

All animal experiments have been approved by Guangxi Medical University Cancer Hospital's Ethical Committee with an approval number: LW2024123.

## Funding

This research was funded by National Natural Science Foundation of China, grant number 82160341 and 82260345, Guangxi Key R&D Program, grant number AB22080066, Guangxi Natural Science Foundation Key Project, grant number 2022GXNSFDA035060, Guangxi Science and Technology Base and Talent Special Project, grant number AD19245197, China Postdoctoral Science Foundation, grant number 2024M750452, Postdoctoral Fellowship Program of CPSF, grant number BX20230068, Joint Project on Regional High-Incidence Diseases Research of Guangxi Natural Science Foundation, grant number 2023JJB140332.

## Declaration of competing interest

The authors declare that they have no known competing financial interests or personal relationships that could have appeared to influence the work reported in this paper.

## Acknowledgments

We greatly appreciate for the support from Guangxi Key Laboratory of Early Prevention and Treatment for Regional High Frequency Tumor.

## Appendix A. Supplementary data

Supplementary data to this article can be found online at https://doi.org/10.1016/j.mtbio.2024.101326.

## Data availability

Data will be made available on request.

## References

[1] R.L. Siegel, A.N. Giaquinto, A. Jemal, Cancer statistics, CA: a cancer journal for clinicians 2024 74 (1) (2024) 12–49.
[2] H. Qiu, S. Cao, R. Xu, Cancer incidence, mortality, and burden in China: a time-trend analysis and comparison with the United States and United Kingdom based on the global epidemiological data released in 2020, Cancer Commun. 41 (10) (2021) 1037–1048.
[3] E. Dekker, P.J. Tanis, J.L.A. Vleugels, P.M. Kasi, M.B. Wallace, Colorectal cancer, Lancet (London, England) 394 (10207) (2019) 1467–1480.
[4] S. Al Bitar, M. El-Sabban, S. Doughan, W. Abou-Kheir, Molecular mechanisms targeting drug-resistance and metastasis in colorectal cancer: updates and beyond, World J. Gastroenterol. 29 (9) (2023) 1395–1426.
[5] A.E. Shin, F.G. Giancotti, A.K. Rustgi, Metastatic colorectal cancer: mechanisms and emerging therapeutics, Trends Pharmacol. Sci. 44 (4) (2023) 222–236.
[6] Y. Asaoka, H. Ijichi, K. Koike, PD-1 blockade in tumors with mismatch-repair deficiency, N. Engl. J. Med. 373 (20) (2015) 1979.
[7] Z. Payandeh, S. Khalili, M.H. Somi, M. Mard-Soltani, A. Baghbanzadeh, K. Hajiasgharzadeh, N. Samadi, B. Baradaran, PD-1/PD-L1-dependent immune response in colorectal cancer, J. Cell. Physiol. 235 (7–8) (2020) 5461–5475.
[8] C. Xu, Y. Liu, Y. Zhang, L. Gao, The role of a cuproptosis-related prognostic signature in colon cancer tumor microenvironment and immune responses, Front. Genet. 13 (2022) 928105.
[9] Q. Song, R. Zhou, F. Shu, W. Fu, Cuproptosis scoring system to predict the clinical outcome and immune response in bladder cancer, Front. Immunol. 13 (2022) 958368.
[10] G. Wang, R. Xiao, S. Zhao, L. Sun, J. Guo, W. Li, Y. Zhang, X. Bian, W. Qiu, S. Wang, Cuproptosis regulator-mediated patterns associated with immune infiltration features and construction of cuproptosis-related signatures to guide immunotherapy, Front. Immunol. 13 (2022) 945516.
[11] Y. Huang, D. Yin, L. Wu, Identification of cuproptosis-related subtypes and development of a prognostic signature in colorectal cancer, Sci. Rep. 12 (1) (2022) 17348.
[12] P. Tsvetkov, S. Coy, B. Petrova, M. Dreishpoon, A. Verma, M. Abdusamad, J. Rossen, L. Joesch-Cohen, R. Humeidi, R.D. Spangler, J.K. Eaton, E. Frenkel, M. Kocak, S.M. Corsello, S. Lutsenko, N. Kanarek, S. Santagata, T.R. Golub, Copper induces cell death by targeting lipoylated TCA cycle proteins, Science (New York, N.Y.) 375 (6586) (2022) 1254–1261.
[13] P.A. Cobine, D.C. Brady, Cuproptosis: cellular and molecular mechanisms underlying copper-induced cell death, Mol. Cell 82 (10) (2022) 1786–1787.
[14] X.-K. Jin, J.-L. Liang, S.-M. Zhang, Q.-X. Huang, S.-K. Zhang, C.-J. Liu, X.-Z. Zhang, Orchestrated copper-based nanoreactor for remodeling tumor microenvironment to amplify cuproptosis-mediated anti-tumor immunity in colorectal cancer, Mater. Today 68 (2023) 108–124.
[15] A.P. West, G.S. Shadel, S. Ghosh, Mitochondria in innate immune responses, Nat. Rev. Immunol. 11 (6) (2011) 389–402.
[16] X. Yu, B. Li, J. Yan, W. Li, H. Tian, G. Wang, S. Zhou, Y. Dai, Cuproptotic nanoinducer-driven proteotoxic stress potentiates cancer immunotherapy by activating the mtDNA-cGAS-STING signaling, Biomaterials 307 (2024) 122512.
[17] Q. Xue, R. Kang, D.J. Klionsky, D. Tang, J. Liu, X. Chen, Copper metabolism in cell death and autophagy, Autophagy 19 (8) (2023) 2175–2195.
[18] X. Zhang, X.C. Bai, Z.J. Chen, Structures and mechanisms in the cGAS-STING innate immunity pathway, Immunity 53 (1) (2020) 43–53.
[19] D. Wang, T. Nie, C. Huang, Z. Chen, X. Ma, W. Fang, Y. Huang, L. Luo, Z. Xiao, Metal-Cyclic dinucleotide nanomodulator-stimulated STING signaling for strengthened radioimmunotherapy of large tumor, Small 18 (41) (2022) e2203227.
[20] M. Tarin, M. Babaie, H. Eshghi, M.M. Matin, A.S. Saljooghi, Elesclomol, a copper-transporting therapeutic agent targeting mitochondria: from discovery to its novel applications, J. Transl. Med. 21 (1) (2023) 745.
[21] G. Yang, L. Xu, Y. Chao, J. Xu, X. Sun, Y. Wu, R. Peng, Z. Liu, Hollow MnO(2) as a tumor-microenvironment-responsive biodegradable nano-platform for combination therapy favoring antitumor immune responses, Nat. Commun. 8 (1) (2017) 902.
[22] M. Cheng, Y. Yu, W. Huang, M. Fang, Y. Chen, C. Wang, W. Cai, S. Zhang, W. Wang, W. Yan, Monodisperse hollow MnO(2) with biodegradability for efficient targeted drug delivery, ACS Biomater. Sci. Eng. 6 (9) (2020) 4985–4992.
[23] J. Ou, H. Tian, J. Wu, J. Gao, J. Jiang, K. Liu, S. Wang, F. Wang, F. Tong, Y. Ye, L. Liu, B. Chen, X. Ma, X. Chen, F. Peng, Y. Tu, MnO(2)-Based nanomotors with active fenton-like Mn(2+) delivery for enhanced chemodynamic therapy, ACS Appl. Mater. Interfaces 13 (32) (2021) 38050–38060.
[24] C. Wang, Y. Guan, M. Lv, R. Zhang, Z. Guo, X. Wei, X. Du, J. Yang, T. Li, Y. Wan, X. Su, X. Huang, Z. Jiang, Manganese increases the sensitivity of the cGAS-STING

pathway for double-stranded DNA and is required for the host defense against DNA viruses, Immunity 48 (4) (2018) 675–687.e7.
[25] M. Nagai, N.H. Vo, L. Shin Ogawa, D. Chimmanamada, T. Inoue, J. Chu, B. C. Beaudette-Zlatanova, R. Lu, R.K. Blackman, J. Barsoum, K. Koya, Y. Wada, The oncology drug elesclomol selectively transports copper to the mitochondria to induce oxidative stress in cancer cells, Free Radic. Biol. Med. 52 (10) (2012) 2142–2150.
[26] J. Fang, W. Islam, H. Maeda, Exploiting the dynamics of the EPR effect and strategies to improve the therapeutic effects of nanomedicines by using EPR effect enhancers, Adv. Drug Deliv. Rev. 157 (2020) 142–160.
[27] H. Kang, L. Chen, Q. Li, H. Chen, L. Zhang, Dual-oxygenation/dual-fenton synergistic photothermal/chemodynamic/starvation therapy for tumor treatment, ACS Appl. Mater. Interfaces 15 (12) (2023) 15129–15139.
[28] W. Xu, X. Qing, S. Liu, D. Yang, X. Dong, Y. Zhang, Hollow mesoporous manganese oxides: application in cancer diagnosis and therapy, Small 18 (15) (2022) e2106511.
[29] F. Hu, J. Huang, T. Bing, W. Mou, D. Li, H. Zhang, Y. Chen, Q. Jin, Y. Yu, Z. Yang, Stimulus-responsive copper complex nanoparticles induce cuproptosis for augmented cancer immunotherapy, Adv. Sci. 11 (13) (2024) e2309388.
[30] S. Lu, Y. Li, Y. Yu, Glutathione-scavenging celastrol-Cu nanoparticles induce self-amplified cuproptosis for augmented cancer immunotherapy, Adv. Mater. 36 (35) (2024) e2404971.
[31] D. Tang, X. Chen, G. Kroemer, Cuproptosis: a copper-triggered modality of mitochondrial cell death, Cell Res. 32 (5) (2022) 417–418.
[32] J. Xia, C. Hu, Y. Ji, M. Wang, Y. Jin, L. Ye, D. Xie, S. Jiang, R. Li, Z. Hu, J. Dai, Copper-loaded nanoheterojunction enables superb orthotopic osteosarcoma therapy via oxidative stress and cell cuproptosis, ACS Nano 17 (21) (2023) 21134–21152.
[33] H. Tian, J. Duan, B. Li, S. Qin, E.C. Nice, W. Zhang, T. Lang, H. Zhang, C. Huang, Clinical chemotherapeutic agent coordinated copper-based nanoadjuvants for efficiently sensitizing cancer chemo-immunotherapy by cuproptosis-mediated mitochondrial metabolic reprogramming, Adv. Funct. Mater. 33 (51) (2023) 2306584.
[34] G. Qiu, D. Wang, P. Xie, Z. Li, N. Zhou, X. Zhang, X. Wang, J. Tang, J. Cao, J. Liu, Harnessing bimetallic iMWA nanosensitizer to unleash ferroptosis and calcium overload: unlocking tumor vulnerability for potentiated iMWA therapy against hepatocellular carcinoma, Chem. Eng. J. (2024) 153368.
[35] Y. Deng, D. Wang, W. Zhao, G. Qiu, X. Zhu, Q. Wang, T. Qin, J. Tang, J. Jiang, N. Lin, L. Wei, Y. Liu, Y. Xie, J. Chen, L. Deng, J. Liu, A Multifunctional Nanocatalytic Metal-Organic Framework as a Ferroptosis Amplifier for Mild Hyperthermia Photothermal Therapy, vol. 7, Research (Wash D C), 2024, p. 397.
[36] E. Falcone, A.G. Ritacca, S. Hager, H. Schueffl, B. Vileno, Y. El Khoury, P. Hellwig, C.R. Kowol, P. Heffeter, E. Sicilia, P. Faller, Copper-catalyzed glutathione oxidation is accelerated by the anticancer thiosemicarbazone Dp44mT and further boosted at lower pH, J. Am. Chem. Soc. 144 (32) (2022) 14758–14768.
[37] Y. Li, J. Yang, Q. Zhang, S. Xu, W. Sun, S. Ge, X. Xu, M.J. Jager, R. Jia, J. Zhang, X. Fan, Copper ionophore elesclomol selectively targets GNAQ/11-mutant uveal melanoma, Oncogene 41 (27) (2022) 3539–3553.
[38] D. Wang, X. Zhu, X. Wang, Q. Wang, K. Yan, G. Zeng, G. Qiu, R. Jiao, X. Lin, J. Chen, Q. Yang, W. Qin, J. Liu, K. Zhang, Y. Liu, Multichannel sonocatalysis amplifiers target IDH1-mutated tumor plasticity and attenuate ros tolerance to repress malignant cholangiocarcinoma, Adv. Funct. Mater. 33 (48) (2023).
[39] M. Shen, Y. Wang, T. Bing, Y. Tang, X. Liu, Y. Yu, Alendronate triggered dual-cascade targeting prodrug nanoparticles for enhanced tumor penetration and STING activation of osteosarcoma, Adv. Funct. Mater. 33 (49) (2023).
[40] L. Hou, C. Tian, Y. Yan, L. Zhang, H. Zhang, Z. Zhang, Manganese-based nanoactivator optimizes cancer immunotherapy via enhancing innate immunity, ACS Nano 14 (4) (2020) 3927–3940.
[41] X. Sun, Y. Zhang, J. Li, K.S. Park, K. Han, X. Zhou, Y. Xu, J. Nam, J. Xu, X. Shi, L. Wei, Y.L. Lei, J.J. Moon, Amplifying STING activation by cyclic dinucleotide-manganese particles for local and systemic cancer metalloimmunotherapy, Nat. Nanotechnol. 16 (11) (2021) 1260–1270.
[42] L. Cai, Y. Wang, Y. Chen, H. Chen, T. Yang, S. Zhang, Z. Guo, X. Wang, Manganese (ii) complexes stimulate antitumor immunity via aggravating DNA damage and activating the cGAS-STING pathway, Chem. Sci. 14 (16) (2023) 4375–4389.
[43] X. Liu, M. Shen, T. Bing, X. Zhang, Y. Li, Q. Cai, X. Yang, Y. Yu, A bioactive injectable hydrogel regulates tumor metastasis and wound healing for melanoma via NIR-light triggered hyperthermia, Adv. Sci. 11 (26) (2024) e2402208.
[44] S.R. Woo, M.B. Fuertes, L. Corrales, S. Spranger, M.J. Furdyna, M.Y. Leung, R. Duggan, Y. Wang, G.N. Barber, K.A. Fitzgerald, M.L. Alegre, T.F. Gajewski, STING-dependent cytosolic DNA sensing mediates innate immune recognition of immunogenic tumors, Immunity 41 (5) (2014) 830–842.
[45] S.M. Harding, J.L. Benci, J. Irianto, D.E. Discher, A.J. Minn, R.A. Greenberg, Mitotic progression following DNA damage enables pattern recognition within micronuclei, Nature 548 (7668) (2017) 466–470.
[46] X. Jin, H. Yang, Z. Mao, B. Wang, Cathepsin B-responsive multifunctional peptide conjugated gold nanorods for mitochondrial targeting and precise photothermal cancer therapy, J. Colloid Interface Sci. 601 (2021) 714–726.
[47] L. Liu, H. Lei, G. Hou, L. Zhang, Y. Chen, Y. Lu, Z. Pei, J. Ge, J. Wu, J. Zhou, L. Cheng, Gas-amplified metalloimmunotherapy with dual activation of pyroptosis and the STING pathway for remodeling the immunosuppressive cervical cancer microenvironment, ACS Nano 18 (20) (2024) 12830–12844.
[48] H. Lei, Q. Li, G. Li, T. Wang, X. Lv, Z. Pei, X. Gao, N. Yang, F. Gong, Y. Yang, G. Hou, M. Chen, J. Ji, Z. Liu, L. Cheng, Manganese molybdate nanodots with dual amplification of STING activation for "cycle" treatment of metalloimmunotherapy, Bioact. Mater. 31 (2024) 53–62.
[49] H. Wu, Z. Zhang, Y. Cao, Y. Hu, Y. Li, L. Zhang, X. Cao, H. Wen, Y. Zhang, H. Lv, X. Jin, A self-amplifying ROS-responsive nanoplatform for simultaneous cuproptosis and cancer immunotherapy, Adv. Sci. 11 (23) (2024) e2401047.
[50] B.W. MacNabb, X. Chen, S. Tumuluru, J. Godfrey, D.N. Kasal, J. Yu, M.L. M. Jongsma, R.M. Spaapen, D.E. Kline, J. Kline, Dendritic cells can prime anti-tumor CD8(+) T cell responses through major histocompatibility complex cross-dressing, Immunity 55 (11) (2022) 2206–2208.
[51] D. Wang, M. Zhang, G. Qiu, C. Rong, X. Zhu, G. Qin, C. Kong, J. Zhou, X. Liang, Z. Bu, J. Liu, T. Luo, J. Yang, K. Zhang, Extracellular matrix viscosity reprogramming by in situ Au bioreactor-boosted microwavegenetics disables tumor escape in CAR-T immunotherapy, ACS Nano 17 (6) (2023) 5503–5516.
[52] A. Mantovani, F. Marchesi, A. Malesci, L. Laghi, P. Allavena, Tumour-associated macrophages as treatment targets in oncology, Nat. Rev. Clin. Oncol. 14 (7) (2017) 399–416.
[53] D. Wang, G. Qiu, X. Zhu, Q. Wang, C. Zhu, C. Fang, J. Liu, K. Zhang, Y. Liu, Macrophage-inherited exosome excise tumor immunosuppression to expedite immune-activated ferroptosis, J Immunother Cancer 11 (5) (2023).
[54] A. Mantovani, P. Allavena, F. Marchesi, C. Garlanda, Macrophages as tools and targets in cancer therapy, Nat. Rev. Drug Discov. 21 (11) (2022) 799–820.